Article | Open Access

Energy Z

Niu *et al. Energy Z* **2026**, 2, 200017 **DOI:**10.20517/energyz.2026.27

Hole transport layers regulate polaron formation in perovskite solar cells

Xiaoran Niu[1,#], Peide Zhu[2,#], Ruoying Pang[1], Shuai Wang[1], Jie Zeng[2], Yong Zhang[3,*], Baomin Xu[2], Feng He[1,*]

Keywords:
Perovskite solar cells, hole transport layers, polaron

Citation: Niu, X.; Zhu, P.; Pang, R.; Wang, S.; Zeng, J.; Zhang, Y.; Xu, B.; He, F. Hole transport layers regulate polaron formation in perovskite solar cells. *Energy Z* **2026**, *2*, 200017. https://dx.doi.org/10.20517/energyz.2026.27

Received: 11 Jun 2026
First Decision: 15 Jul 2026
Revised: 22 Jul 2026
Accepted: 3 Aug 2026
Published: 31 Aug 2026

Academic Editor:
Qingdong Zheng
Copy Editor:
Shu-Yuan Duan
Production Editor:
Shu-Yuan Duan

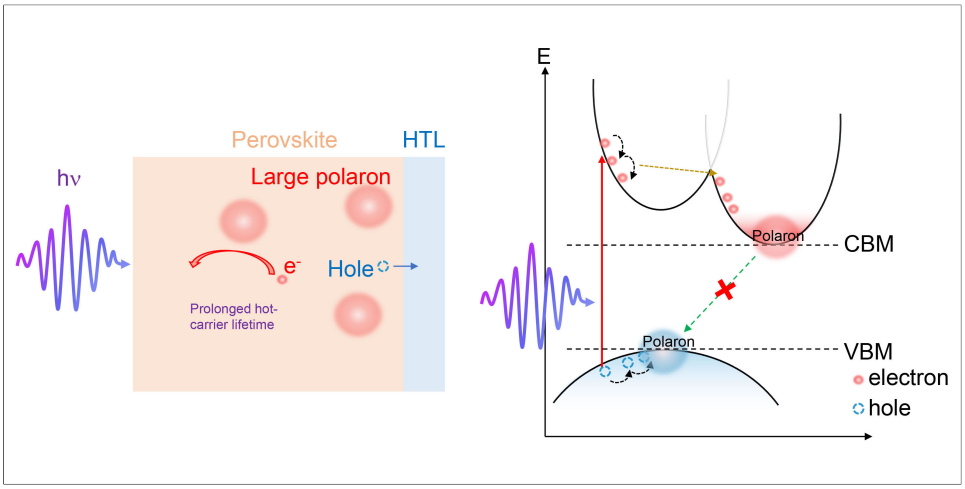

Abstract

The mechanisms by which hole transport layers (HTLs) regulate carrier relaxation and polaron formation at perovskite interfaces remain poorly understood, despite their critical role in determining photovoltaic performance. Here, we combine transient absorption spectroscopy and time-resolved photoluminescence to elucidate the HTL-dependent carrier dynamics of metal halide perovskites. We show that Poly[bis(4-phenyl)(2,4,6-triMethylphenyl)aMine] (PTAA) promotes interfacial non-radiative recombination, while [2-(9H-carbazol-9-yl)ethyl]phosphonic acid (2-PACz) passivates interfacial defects and facilitates carrier transfer across the perovskites/HTL interface, resulting in accelerated ground-state bleach recovery. Under high excitation fluences, a second ground-state bleach (GSB2) emerges that is consistent with HTL-facilitated polaron formation, revealing an additional carrier-relaxation pathway. The associated polaronic screening suppresses electron-hole Coulomb interactions and sustains hot-carrier populations over extended timescales. These spectroscopic insights directly correlate with device performance:

Check for updates

[1]National Key Laboratory of Laser Spatial Information, Guangdong Provincial Key Laboratory of Aerospace Communication and Networking Technology, Guangdong Provincial Key Laboratory of Integrated Photonic-Electronic Chip, Harbin Institute of Technology (Shenzhen), Shenzhen 518055, Guangdong, China.
[2]Department of Materials Science and Engineering, Southern University of Science and Technology, Shenzhen 518055, Guangdong, China.
[3]Sustainable Energy and Environment Thrust, Function Hub, The Hong Kong University of Science and Technology (Guangzhou), Guangzhou 511400, Guangdong China.
[#]These authors contributed equally to this work.

[*]**Correspondence to:** Prof. Yong Zhang, The Hong Kong University of Science and Technology (Guangzhou), Guangzhou 511400, Guangdong, China. E-mail: yongzhang@hkust-gz.edu.cn; Prof. Feng He, Harbin Institute of Technology (Shenzhen), Shenzhen 518055, Guangdong, China. E-mail: hefeng2020@hit.edu.cn

2-PACz-based perovskite solar cells achieve a power conversion efficiency of 26.03% under 1-sun illumination and 27.24% under 5-sun concentration, outperforming PTAA-based counterparts. Our findings establish interfacial control of polaron formation as a design principle for simultaneously regulating carrier relaxation and photovoltaic performance in perovskite solar cells.

INTRODUCTION

Metal halide perovskites (MHPs) have revolutionized optoelectronics with their exceptional properties, such as low carrier recombination rates, long-range charge diffusion[1-4], and inherent defect tolerance[5,6]. These features enable applications in efficient and cost-effective large-scale solar cells[7,8], solid-state lighting[9,10], and spintronic devices[11]. A crucial component in MHP-based devices, particularly in inverted perovskite solar cells (PSCs), is the hole transport layer (HTL), which influences perovskite crystallization and interfacial stability[12-15]. Traditional HTLs in PSCs often utilize polymers such as poly(3,4-ethylenedioxythiophene):poly(styrenesulfonate) (PEDOT:PSS) and Poly[bis(4-phenyl)(2,4,6-triMethylphenyl)aMine] (PTAA), which have demonstrated strong performance but present challenges in terms of stability and device longevity[16]. PEDOT:PSS, for instance, is hygroscopic and acidic, impacting device durability, whereas PTAA's hydrophobic nature complicates large-area perovskite deposition. Alternative inorganic HTLs, such as NiO_x, offer greater stability and compatibility with scalable fabrication but may induce interfacial losses due to non-radiative recombination centers[17]. Recent approaches to improving HTL effectiveness focus on structural modifications, interfacial treatments, and self-assembled monolayer (SAM)-based hole-selective contacts[12]. SAM-based contacts, with their customizable anchoring and functional groups, enable better energy alignment and efficient hole extraction[12]. Among the numerous HTLs developed for inverted perovskite solar cells, PTAA and [2-(9H-carbazol-9-yl)ethyl]phosphonic acid (2-PACz) represent two fundamentally different interface engineering strategies. PTAA forms a polymeric van der Waals contact with the perovskite, whereas 2-PACz forms a chemically bonded self-assembled monolayer that effectively passivates interfacial defects and tailors the interfacial energetics. While these materials have been widely studied for device optimization and defect passivation, whether HTL chemistry fundamentally alters high-density carrier relaxation and polaron formation remains largely unexplored. Recent studies have further highlighted that interpreting interfacial charge-transfer processes in perovskites requires careful distinction between defect passivation, non-radiative recombination, and charge extraction. In particular, steady-state photoluminescence (PL) primarily reflects quasi-Fermi level splitting and interfacial recombination losses, whereas charge extraction is more reliably evaluated using transient spectroscopic techniques or bias-dependent optical measurements. These considerations motivate a comprehensive investigation of HTL-dependent carrier dynamics across multiple timescales[18,19].

In a comparative study of photoexcited carrier dynamics in pristine perovskite (PVK), PVK coated with PTAA (denoted as PVK/PTAA), and PVK coated with 2-PACz (denoted as PVK/2-PACz) films using steady-state PL, time-resolved PL (TRPL), and transient absorption spectroscopy (TAS), we identify a pronounced contrast in interfacial energetics that govern hole extraction. PTAA and 2-PACz induce markedly different interfacial photophysics. While PTAA is associated with enhanced interfacial non-radiative recombination, the self-assembled 2-PACz monolayer effectively passivates interfacial defects and promotes carrier transfer across the PVK/HTL interface. By combining excitation-geometry-dependent TRPL with TAS measurements, we disentangle the roles of interfacial passivation and carrier extraction and reveal a high-fluence carrier-relaxation pathway that is consistent with HTL-facilitated polaron formation. Device measurements further correlate these interfacial processes with photovoltaic performance improvements. Together, these findings demonstrate that HTL-engineered interfaces not only dictate charge-transfer pathways but also modulate polaron formation under high carrier densities, ultimately enabling more efficient and stable perovskite photovoltaics.

EXPERIMENTAL

Materials

Formamidine acetate (FAAc, 99%), cesium acetate (CsAc, 99%), methylamine (MA, AR, 30-33 wt.% in ethanol), and lead acetate trihydrate ($PbAc_2 \cdot 3H_2O$, AR, 99.5%) were purchased from Aladdin. Hydroiodic acid (HI, 47 wt.% in water) was purchased from Macklin. PbI_2 (98%) was acquired from TCI (Shanghai) Development Co., Ltd. 2-PACz, PTAA, 2,9-Dimethyl-4,7-diphenyl-1,10-phenanthroline (BCP, 99.9%), methylammonium chloride (MACl, > 99.5%), piperazinium iodide (PI, 99%), C_{60} (99.9%), and phenmethylammonium iodide (PMAI, 99.9%) were bought from Xi'an Yuri Solar Technology Co., Ltd. Cu (99.999%) were purchased from Fuzhou Innovation Photoelectric Technology Co. Ltd. N', N'-Dimethylformamide (DMF, 99.8%), isopropanol (IPA, 99.5%), chlorobenzene (CB, 99.8%), dimethyl sulfoxide (DMSO, 99.9%) were obtained from J&K Scientific Co., Ltd. All chemicals were used as received, without additional purification.

Perovskite precursor preparation

The perovskite $CsPbI_3$, $MAPbI_3$, and $FAPbI_3$ microcrystals were synthesized using our previously established work[7].

Perovskite solar cells fabrication

Deice configuration: ITO/2-PACz or PTAA/$FA_{0.85}MA_{0.1}Cs_{0.05}PbI_3$/$C_{60}$/BCP/Cu

The perovskite precursor solution was prepared at a concentration of 1.65 M by mixing $CsPbI_3$, $MAPbI_3$, and $FAPbI_3$ in DMF/DMSO (4:1, v/v) according to the stoichiometric ratio $(FAPbI_3)_{0.85}(MAPbI_3)_{0.1}(CsPbI_3)_{0.05}$. Additionally, 0.5 mol% PMAI, 8 mol% MACl, and 3 mol% excess PbI_2 were supplemented to control the crystallization process. The synthesis of perovskite microcrystals followed our previously established procedure[7].

Indium tin oxide (ITO) glass substrates (1.5 × 1.5 cm^2) with a sheet resistance of 12 Ω/sq were utilized. The cleaning process involved three repetitive sonication steps, each consisting of sequential immersion in deionized water and isopropanol for 20 min per solvent. Following drying, the substrates were subjected to UV-ozone treatment for 20 min. A hole-transporting layer (HTL) of 2-PACz was deposited onto the substrates by spin-coating 40 μL of a 0.8 mg/mL solution in isopropanol (IPA) at 5,000 rpm for 60 s. Separately, a PTAA-HTL was deposited by spin-coating 40 μL of a 0.8 mg/mL solution in chlorobenzene (CB) under the same conditions (5,000 rpm, 60 s). The HTL-deposited substrates were annealed at 100 °C for 10 min. The perovskite precursor solution was deposited by spin-coating at 5,000 rpm for 30 s. During the spin process, 180 μL of CB was introduced as an anti-solvent at 12 s. The resultant films were then thermally annealed at 100 °C for 30 min. For surface defect passivation, a piperazinium iodide solution (0.5 mg/mL in IPA) was applied, followed by a secondary annealing step at 100 °C for 5 min. The device fabrication was finalized by the sequential thermal evaporation of C_{60} (30 nm), BCP (8 nm), and copper (100 nm) under a vacuum pressure of 2 × 10^{-5} Torr. The deposition rates were maintained at 0.3 Å/s for the electron-transporting layers (C_{60} and BCP) and 1.0 Å/s for the copper electrode.

Perovskite solar cells characterizations

A Keithley 2400 source meter and a Newport solar simulator (Enlitech Solar Simulator SS-F7-3A) were employed to characterize the device performance under standard AM 1.5G conditions (100 mW cm^{-2}). The light intensity was precisely calibrated using a NIST-certified single-crystal Si solar cell (Newport 532 ISO1599).

Perovskite characterization

An FLS1000 spectrometer (Edinburgh Instruments Ltd.) equipped with an Xe lamp was employed to measure steady-state PL spectra. TRPL decay kinetics were recorded at 787 nm with an excitation wavelength of 468 nm. The photoluminescence was excited from the perovskite side of the PVK/ITO substrate configuration. TRPL measurements were performed under two excitation geometries. The excitation laser was incident either from the perovskite side or from the HTL side, allowing comparison of carrier dynamics at the two interfaces. An ultrafast transient absorption spectrometer (Time-tech Spectra Limited Company) was used for TAS measurements. Morphological features were examined by field-emission SEM (SU8230, Hitachi).

RESULTS AND DISCUSSION

Linear spectra

To compare charge carrier dynamics influenced by different hole transport layers, we investigated pristine $(FAPbI_3)_{0.85}(MAPbI_3)_{0.1}(CsPbI_3)_{0.05}$ perovskite (PVK) films as a control sample (for preparation and characterization see Ref.[7]). Additionally, we examined PVK films spin-coated on two distinct HTL materials: PTAA, a commonly used polymeric HTL (denoted as PVK/PTAA), and 2-PACz, a self-assembled monolayer-based HTL (denoted as PVK/2-PACz). These samples allow us to study how HTL materials impact charge carrier behavior, energy alignment, and interfacial properties, providing insights into optimizing HTL designs for improved perovskite optoelectronic devices. Figure 1A presents the linear absorption and PL spectra of the three investigated samples. The steady-state absorption spectra exhibit nearly identical profiles for the pristine PVK film and PVK films with HTLs, with a distinct and sharp absorption edge around 800 nm. Using the Tauc plot method (see Supplementary Figure 1), we determined that the bandgap remains nearly constant across the samples, with values of 1.552 eV, 1.554 eV, and 1.555 eV for pristine PVK, PVK/PTAA, and PVK/2-PACz films, respectively. These results confirm that the addition of HTLs does not significantly impact the intrinsic bandgap of the perovskite material, allowing for a direct comparison of their influence on charge carrier dynamics and interfacial properties. Correspondingly, Figure 1A shows that while the pristine PVK exhibits a PL peak at 792 nm, a slight blue shift is observed in the HTL-coated films. These findings indicate that while the bulk optical properties remain largely unchanged, HTLs subtly influence interfacial electronic properties and carrier dynamics. Notably, the PL intensity decreased tenfold after coating with PTAA, while it increased significantly with 2-PACz, consistent with the reported trend[17,20].

To further assess the influence of different HTLs on interfacial carrier dynamics, TRPL measurements under 468 nm excitation were performed from both the PVK side and the ITO side, as shown in Figure 1B and C. Average carrier lifetimes were extracted through exponential fitting and compared across the three samples in Figure 1D, enabling the separation of intrinsic perovskite recombination from HTL-induced interfacial effects. When excited from the ITO side, the fitted lifetimes for the PVK, PVK/PTAA, and PVK/2-PACz samples are 3,515 ± 21 ns, 81 ± 0.8 ns, and 1,090 ± 8 ns, respectively, compared with 801 ± 6 ns, 75 ± 1.4 ns, and 591 ± 4.6 ns under PVK-side excitation. Compared with PVK-side excitation, pronounced lifetime extensions are observed for the pristine PVK and PVK/2-PACz samples, whereas the PVK/PTAA sample exhibits only a marginal increase. This distinct behavior indicates that the influence of excitation geometry strongly depends on the interfacial properties of the HTL, with 2-PACz effectively modifying interfacial carrier dynamics through defect passivation and carrier transfer, while PTAA shows only a negligible interface-dependent effect. To quantitatively evaluate this asymmetry, we introduce a difference factor $\beta = \frac{\tau_{HTL-side} - \tau_{PVK-side}}{\tau_{PVK-side}}$, which reflects the relative enhancement in carrier lifetime induced by HTL-side excitation.

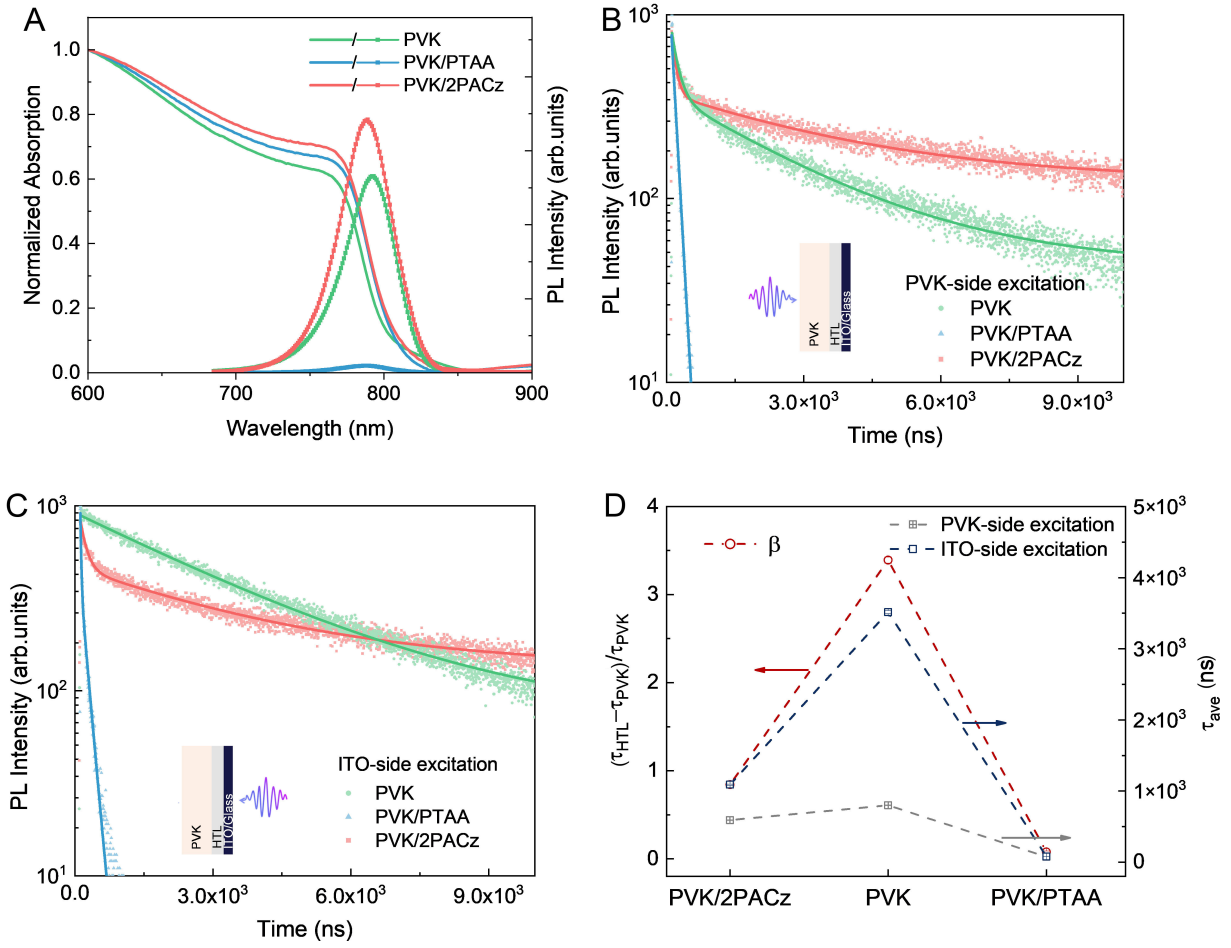

Figure 1. Spectral and photoluminescence characterization. (A) Normalized steady-state absorption spectra (solid lines) and PL spectra (dots and solid lines) of pristine PVK, PVK/PTAA and PVK/2-PACz films. Green: PVK; blue: PVK/PTAA; red: PVK/2-PACz; (B and C) TRPL decay curves monitored at 787 nm under 468 nm excitation (fluence = 0.76 μJ/cm^2), measured from the PVK side (B) and the ITO side (C). Insets: schematic measurement configurations. Green squares: PVK; blue squares: PVK/PTAA; red squares: PVK/2-PACz. Solid lines represent exponential fits; (D) Comparison of TRPL lifetimes for the three sample sets under different excitation geometries. Gray squares: excitation from the PVK side; blue squares: excitation from the ITO side; red circles: difference factor . PVK: Pristine perovskite; PTAA: Poly[bis(4-phenyl)(2,4,6-triMethylphenyl)aMine]; 2-PACz: [2-(9H-carbazol-9-yl)ethyl]phosphonic acid; PL: photoluminescence; ITO: indium tin oxide; TRPL: time-resolved photoluminescence.

Notably, the pure PVK exhibits the highest β value, indicating a much longer lifetime under ITO -side excitation compared to PVK-side excitation. Given that the penetration depth at 468 nm excitation (196 nm) is smaller than the PVK thickness (~ 700 nm), the TRPL response predominantly reflects the recombination characteristics near the excitation surface. The significantly shorter lifetime observed for PVK-side excitation therefore suggests severe non-radiative recombination at the PVK surface, likely arising from a high density of surface defects. In contrast, the PVK/ITO interface shows substantially improved quality, with fewer defect-mediated recombination pathways, leading to reduced non-radiative losses and prolonged carrier lifetimes.

In the PVK/HTL system, however, the PL intensity and carrier lifetime are governed by two competing mechanisms: (i) the HTL provides an efficient pathway for extracting photoexcited holes from the perovskite, which suppresses radiative recombination; and (ii) the HTL can passivate interfacial defect states, reducing non-radiative recombination and thereby enhancing radiative emission. Compared to pristine PVK, the enhanced PL intensity observed in PVK/2-PACz indicates reduced non-radiative recombination

and improved interfacial passivation by 2-PACz, consistent with previous reports[21,22]. We note that steady-state PL intensity primarily reflects quasi-Fermi level splitting and interfacial recombination losses rather than charge-extraction efficiency, as emphasized in recent studies of perovskite optoelectronics[18,19]. Although TRPL lifetimes alone cannot uniquely distinguish extraction from recombination processes, the excitation-geometry-dependent measurements reveal distinct interfacial carrier dynamics. Combined with TAS measurements discussed below, these observations support more efficient interfacial hole transfer in PVK/2-PACz than in PVK/PTAA. When excited from the PVK side, carriers must diffuse towards the PVK/2-PACz interface before transfer occurs, during which scattering and recombination weaken the built-in electric field and slow extraction. In contrast, ITO -side excitation enables ultrafast hole transport directly into 2-PACz, rapidly establishing an interfacial electric field that suppresses further transfer. This screening effect results in a carrier lifetime nearly twice that obtained under PVK-side excitation. For PVK/PTAA, however, the carrier lifetime shows minimal dependence on excitation direction ($\beta \approx 0$), indicating weaker hole extraction and poorer interface passivation compared with 2-PACz. This suggests that PTAA provides limited interfacial improvement and inefficient carrier transfer in contrast to 2-PACz. We note that a rigorous assessment of charge extraction under operating conditions may additionally be obtained through bias-dependent PL measurements that monitor the evolution of emission from open-circuit to short-circuit conditions. Such measurements have recently been proposed as a direct probe of extraction efficiency in perovskite devices[19]. While beyond the scope of the present study, our conclusions regarding carrier transfer are supported by the combined TAS and excitation-geometry-dependent TRPL results.

TA spectra

To understand the impact of HTLs on the photophysical properties of PSCs, we first examined the photoexcited carrier relaxation in the pristine PVK film using TAS. Figure 2A-C present the 2D pseudo-color maps of the TAS under 660 nm excitation with pump fluences ranging from 4.5 to 59.1 μJ/cm^2. The 660 nm pump wavelength was selected to avoid excitation of the HTL in later comparative measurements, ensuring that the observed spectral responses originate solely from the perovskite layer. In the transient absorption (TA) spectra (ΔA/A), negative signals (red) represent ground-state bleach (GSB), while positive signals (blue) correspond to excited-state absorption (ESA). At a fluence of 4.5 μJ/cm^2 [Figure 2A], the absorption depth of perovskite at 660 nm (~ 249.5 nm) yields a carrier density of 6.04×10^{17} cm^{-3}, at which thermal and Auger recombination effects can be safely neglected[23]. The pronounced GSB at 780 nm, which is consistent with the optical bandgap of 1.555 eV (~ 797 nm) extracted from the steady-state absorption spectrum, is therefore attributed to the band filling effect[24,25]. As shown in Supplementary Figure 2, the competition between bandgap renormalization (redshift) and the Burstein-Moss effect (B-M effect, blueshift) leads to a net redshift of the GSB peak at longer timescales. Meanwhile, the weak ESA near 800 nm vanishes within 1 ps and is subsequently overshadowed by the dominant GSB. With increasing pump fluences, as shown in Figure 2B and C, the GSB peak broadens and redshifts, indicating enhanced carrier-carrier interactions that accelerate GSB recovery and promote faster carrier thermalization at higher excitation densities. Notably, when the pump fluence exceeds 22.7 μJ/cm^2, a second ground-state bleach (GSB2) emerges around 815 nm, whose origin will be discussed in the following section.

We further performed global fitting of the TA spectra in Figure 2A-C to extract the corresponding decay-associated spectra (DAS), as shown in Figure 2D-F[26]. In Figure 2D, the fitting of the TA dynamics in Figure 2A reveals two distinct decay components, indicating multiple relaxation pathways. The fast decay component, occurring within the sub-picosecond regime (blue curve), exhibits a spectral profile resembling the first derivative of the absorption band, characteristic of transient band shifts and state filling of accumulated carriers. This behavior is consistent with the instantaneous shift of the absorption band reported previously[26-28], and is therefore assigned to hot-carrier cooling immediately after photoexcitation. In contrast, the slow decay component (orange curve) on the nanosecond timescale displays a red-shifted

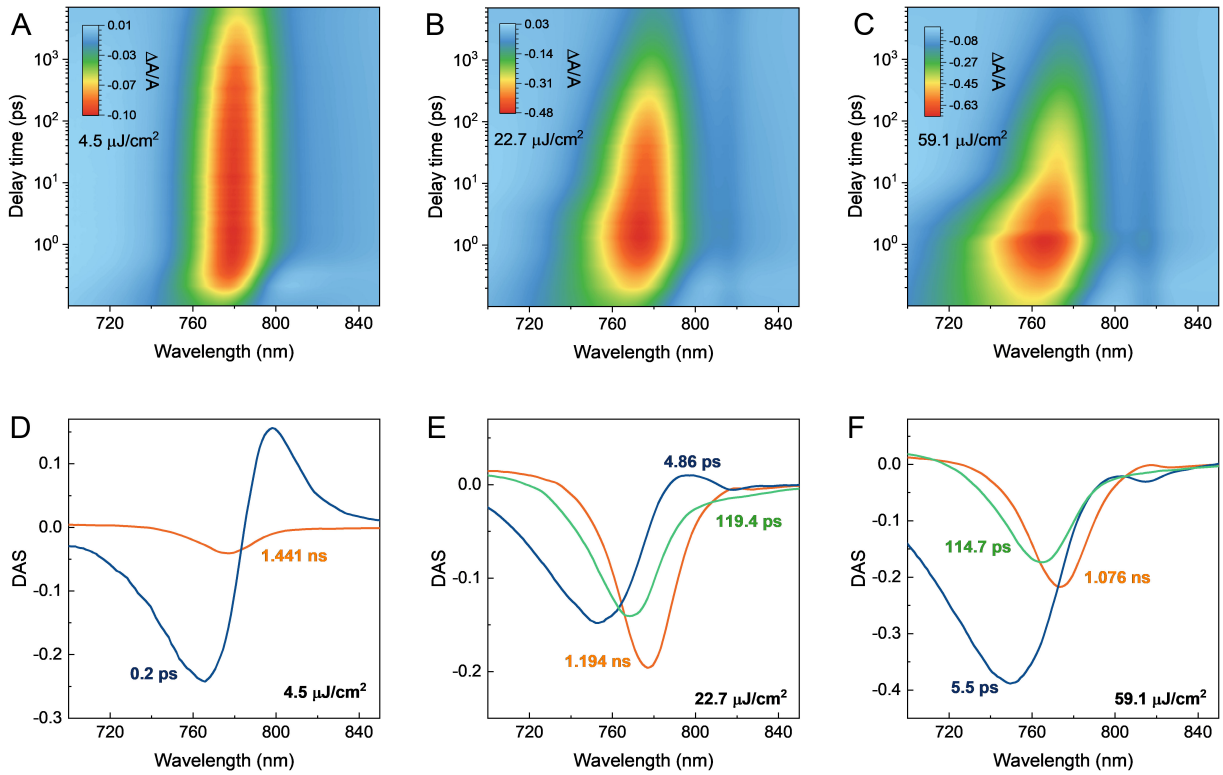

Figure 2. TAS of pristine PVK film under 660 nm excitation. (A-C) 2D pseudo-color plots of TAS at pump fluences of 4.5 μJ/cm² (A), 22.7 μJ/cm² (B), and 59.1 μJ/cm² (C); (D-F) Corresponding DAS extracted from global fitting of the data in (A-C), revealing the characteristic fast and slow decay components at each fluence. TAS: Transient absorption spectroscopy; PVK: pristine perovskite; DAS: decay-associated spectra.

bleach-like spectrum, corresponding to the recovery of the ground state. We attribute this component to bimolecular of photogenerated electrons and holes[29].

At higher fluences, as shown in Figure 2E, three decay components are required to adequately reproduce the TA dynamics. The additional intermediate component (green curve), appearing on the ~ 100 ps timescale, is attributed to Auger recombination based on the following evidence: (i) The carrier density at this fluence reaches 3.02×10^{18} cm^{-3}, where Auger recombination becomes significant and can no longer be neglected[23]; (ii) As shown in Supplementary Figure 3, the ΔA^{-2} kinetics at the GSB peak exhibit a linear dependence after 15 ps[26], indicating that three-body Auger recombination dominates the carrier decay in this time window, whereas the sublinear behavior within the first ~ 15 ps will be discussed later; (iii) As illustrated in Figure 2F, the amplitude of this component decreases with increasing fluence, consistent with enhanced carrier-carrier interactions accelerating the Auger process. Meanwhile, the strengthened carrier interactions at high excitation densities also reduce the slow decay component (orange curve), with its lifetime decreasing from 1.441 ns to 1.076 ns. In contrast, the fast decay component exhibits an extended carrier lifetime at higher fluence, likely due to mechanisms such as the hot phonon bottleneck, giant polaron screening, or acoustic-optical phonon up-conversion[1,30,31]. Notably, the spectral profile of this fast component shows a dip around 815 nm, resembling the shape of a bleach feature. This behavior suggests that the emergence of the GSB2 signal interferes with the hot-carrier cooling pathway, altering the early relaxation dynamics.

To further elucidate the influence of HTLs, we performed TAS measurements on PVK/PTAA and PVK/2-PACz films from the PVK side (see Supplementary Figures 4 and 5). In both cases, the DAS profiles remain largely unchanged across different pump fluences, indicating that incorporating HTLs does not modify the

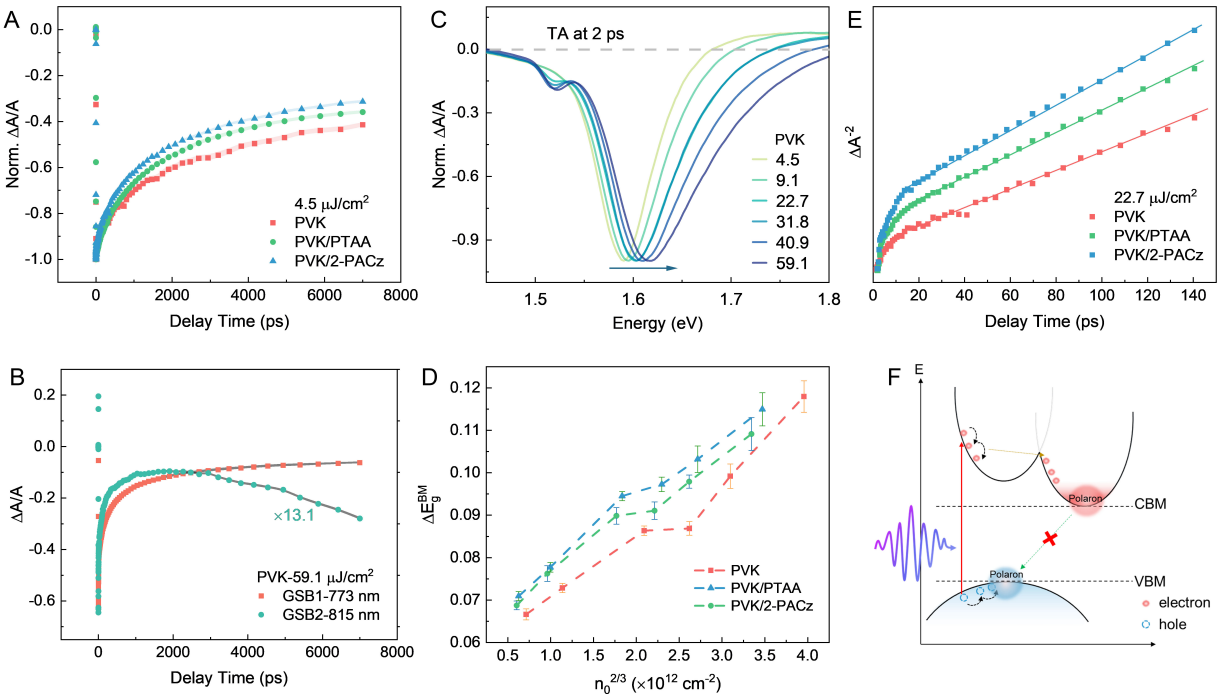

Figure 3. Influence of hole transport layer on ultrafast carrier dynamics. (A) Normalized fs-TA kinetics at the GSB1 position for the pristine PVK, PVK/PTAA, and PVK/2-PACz under 660 nm excitation at a fluence of 4.5 μJ/cm²; (B) TA kinetic curves of GSB1 and GSB2 for the pristine PVK film at a fluence of 59.1 μJ/cm², where the GSB2 signal is scaled by a factor of 13.1 for clarity. Data points are represented by symbols, and the shaded colored regions indicate the standard error derived from three independent measurements performed at different locations on the same sample in both (A) and (B); (C) Normalized TA spectra of the pristine PVK at 2 ps for pump fluences ranging from 4.5 to 59.1 μJ/cm²; (D) Variation of ΔE_g^{BM} as a function of the 2/3 power of the excitation carrier density, extracted from TA spectra at 2 ps. Error bars represent the measurement variability across spatial positions on the same sample; (E) ΔA^{-2} as a function of delay time at GSB1 for pristine PVK, PVK/PTAA, and PVK/2-PACz at 22.7 μJ/cm². The linear region after 15 ps indicates Auger recombination dominance; (F) Schematic illustration of carrier dynamics in perovskite under high carrier density excitation. PVK: Pristine perovskite; PTAA: Poly[bis(4-phenyl)(2,4,6-triMethylphenyl)aMine]; 2-PACz: [2-(9H-carbazol-9-yl)ethyl]phosphonic acid; TA: transient absorption; GSB: ground-state bleach; CBM: conduction band minimum; VBM: valence band maximum.

intrinsic fluence-dependent carrier relaxation pathways in PVK. Instead, the HTLs primarily influence interfacial carrier processes, specifically hole extraction from PVK into the HTL and the first-order Shockley-Reed-Hall recombination at the interface mediated by trap states.

Hole extraction in HTL

To compare the influence of HTLs on ultrafast carrier dynamics, we plotted the normalized TA kinetics at GSB1 under a pump fluence of 4.5 μJ/cm² in Figure 3A. On longer timescales (within 7 ns), PVK/2-PACz exhibits the fastest GSB1 than both pristine PVK and PVK/PTAA. The GSB relaxation is governed by two competing processes: defect-assisted nonradiative recombination and hole transport from PVK into the HTL[32-35]. Although PVK/PTAA shows accelerated decay due to interfacial defects, PVK/2-PACz still decays more rapidly, confirming that efficient hole extraction - not defect-driven recombination - dominates at this low carrier density. Taken together with the excitation-geometry-dependent TRPL measurements, the faster GSB recovery in PVK/2-PACz suggests more efficient interfacial carrier transfer than in PVK/PTAA. Because steady-state PL predominantly reflects interfacial passivation, the TAS results provide complementary evidence that 2-PACz not only suppresses non-radiative recombination but also facilitates carrier extraction across the PVK/HTL interface. As the excitation density increases, however, the decay kinetics of all samples gradually converge as shown in Supplementary Figure 6. This behavior arises from interfacial hole accumulation and the high carrier density within the HTL, which saturates the hole-transfer process and limits further extraction[36], leading to overlapping decay curves.

It is worth noting that even at a high fluence of 59.1 μJ/cm², the HTLs still retain a weak degree of hole extraction. However, this does not directly imply poor device performance, because the extracted holes remain confined within the HTL rather than being collected, as would occur in a full device stack[36]. In complete PSCs, imbalanced electron or hole transport, together with interfacial trap states, can induce charge accumulation at the PVK/HTL interface. Such accumulation reduces the open-circuit voltage and introduces pronounced current-voltage hysteresis, ultimately compromising device stability and operational durability[37]. These observations underscore the importance of interface engineering to suppress trap-assisted barriers and maintain balanced charge extraction, both of which are crucial for pushing PSC efficiencies closer to their theoretical limits.

Polaron formation

The appearance of a second GSB was previously reported by Zheng *et al*. as a new trap-related channel in PVK nanoparticles[26]. In contrast, our observations reveal that GSB2 also emerges in thin-film PVK under high excitation. By tracking GSB2 dynamics at a fluence of 59.1 μJ/cm², we find that its temporal evolution diverges from that of GSB1 after 1,500 ps, as indicated by the green squares in Figure 3B. The GSB2 kinetic trace bends downward at longer delays, indicating that additional energy progressively flows into this channel. For clarity, the GSB2 signal in Figure 3B is scaled by a factor of 13.1.

To further probe the origin of GSB2, we examined the fluence-dependent normalized TA spectra at 2 ps [Figure 3C]. The main bleach peak blue-shifts and broadens with increasing fluence, consistent with the B-M band-filling effect[25]. Interestingly, at intermediate fluences of 22.7 and 31.8 μJ/cm², the spectra show negligible blue-shift or broadening, deviating from the expected B-M trend. According to the B-M model, the bandgap shift scales with carrier density n as follows[38]:

$$\Delta E_g^{BM} = \frac{\hbar^2}{2m_{eh}^*}\left(3\pi^2 n\right)^{2/3} \quad (1)$$

where ΔE_g^{BM} is the B-M shifts, $\hbar$ is the Planck constant, and m_{eh}^* is the reduced effective mass of the photogenerated electron-hole pair. We therefore extracted ΔE_g^{BM} as a function of $n^{2/3}$ from the TA spectra in Figure 3C and Supplementary Figure 7 to quantify deviations from the B-M prediction and identify the onset of GSB2-related processes.

However, as shown in Figure 3D, a plateau in ΔE_g^{BM} appears at $n^{2/3} \sim 2 \times 10^{12}$ cm^{-2} (corresponding to a fluence of 22.7 μJ/cm²) for all three samples. Beyond this plateau, the slope changes. Since this fluence coincides with the onset of GSB2, we attribute the plateau to the emergence of a new relaxation channel associated with GSB2. By analyzing the slope before and after the plateau, we extract the variation in the reduced effective mass m_{eh}^*. Interestingly, m_{eh}^* increases in the PVK/HTL systems but decreases in pristine PVK, suggesting that the HTL modifies the early-time carrier-phonon coupling environment.

To elucidate the origin of this slope change, we further analyzed ΔA^{-2} dynamics for GSB1 at 22.7 μJ/cm² [Figure 3E]. All three samples exhibit a linear ΔA^{-2} dependence from 15-140 ps, confirming that the ~ 110 ps component in the DAS spectra arises from Auger recombination. In contrast, the sublinear behavior within the first 15 ps indicates the involvement of a higher-order process beyond Auger recombination. At these high carrier densities, excess charges (either electrons or holes) can strongly couple to ionic vibrations, forming large polarons[39]. Polaron formation modifies the carrier scattering landscape, increases the effective mass, and alters subsequent relaxation pathways[40].

We therefore propose that the emergence of GSB2 at high fluence is consistent with polaron formation. Alternative explanations, including simple band filling, local heating, and carrier-carrier interactions, are unlikely to fully account for the appearance of a distinct bleach feature with markedly different temporal dynamics. The associated lattice distortion may be related to previously reported Rashba spin splitting in highly excited perovskites[41-44], thereby opening an additional carrier-relaxation channel from the GSB1 (1.60 eV) to the lower-energy GSB2 (1.52 eV), as illustrated in Figure 3F. This mechanism explains the anomalous long-lived behavior of GSB2 in Figure 3B: once carriers accumulate in this polaron-mediated channel, the resulting screening suppresses Coulomb interactions, thereby slowing recombination and preventing GSB2 relaxation back to the ground state within our detection window. The extended persistence of carriers in this "hot" polaronic channel suggests that such states may be advantageous for long-range transport and extraction into the adjacent HTL.

In pristine PVK, polarons exhibit strong repulsive interactions when oppositely charged species remain spatially separated, and the resulting dielectric screening is pronounced. However, as the excitation density increases beyond the threshold fluence of 22.7 μJ/cm², the average polaron-polaron spacing decreases to the point where their wavefunctions begin to overlap. This overlap drives a transition from repulsive to attractive interactions[39], which accelerates the recombination of oppositely charged polarons. Consequently, the reduced effective mass decreases above this threshold. Meanwhile, the presence of polarons is known to impede hot-carrier cooling[44,45], consistent with our observation that the fast decay component in the DAS becomes slower with increasing excitation intensity.

When a HTL is introduced, efficient hole extraction reduces the population of positively charged polarons within the PVK layer, causing electron-induced lattice distortion to dominate the polaronic landscape. As the carrier density continues to rise, the effective special volume available to electron polarons becomes larger relative to that in pristine PVK, and therefore the system does not undergo the same repulsion-to-attraction transition. Instead, in the PVK/HTL structure, m^*_{eh} increases beyond the 22.7 μJ/cm² threshold.

This contrasting behavior originates from HTL-induced electron-hole separation at the PVK/HTL interface, which establishes a local electric field that perturbs free diffusion. The resulting spatially nonuniform carrier distribution increases the probability of carrier localization, thereby strengthening electron-lattice interactions[46]. These interactions stabilize polaronic states and prevent their collapse even at high carrier densities. As a result, no decrease in the effective mass is observed across the accessible excitation range. Such polaron-stabilizing behavior could be further resolved using advanced nano-imaging techniques[47].

Device performance

The inverted perovskite solar cells employed in this work for comparative performance analysis had the device architecture ITO/HTL/PVK/C_{60}/BCP/Cu, as schematically represented in Figure 4A. A cross-sectional scanning electron microscopy (SEM) view of the complete device architecture is displayed in Figure 4B. The current density-voltage (*J*-*V*) characteristics of PTAA-based and 2-PACz-based PSCs are shown in Figure 4C, with devices without an HTL included for comparison. The corresponding photovoltaic parameters are summarized in Table 1. Among all the fabricated devices, the PVK/2-PACz-based PSC achieved the highest performance, which yielded a power conversion efficiency (PCE) of 26.03% with a short-circuit current (J_{SC}) of 25.16 mA/cm² and an open-circuit voltage (V_{OC}) of 1.20 V. In contrast, the PVK/PTAA-based device reaches a PCE of 23.12%. The V_{OC} deficits of the 2-PACz- and PTAA-based devices are 0.355 V and 0.404 V, respectively, highlighting the superior voltage management enabled by 2-PACz.

As shown in Figure 4D, MPP tracking of the champion 2-PACz-based device was performed under continuous AM 1.5G illumination with an applied bias of 1.06 V over 600 s, yielding a stabilized efficiency of 25.89%. Device reproducibility was evaluated across 40 devices [Figure 4E]. The 2-PACz-based PSCs exhibit

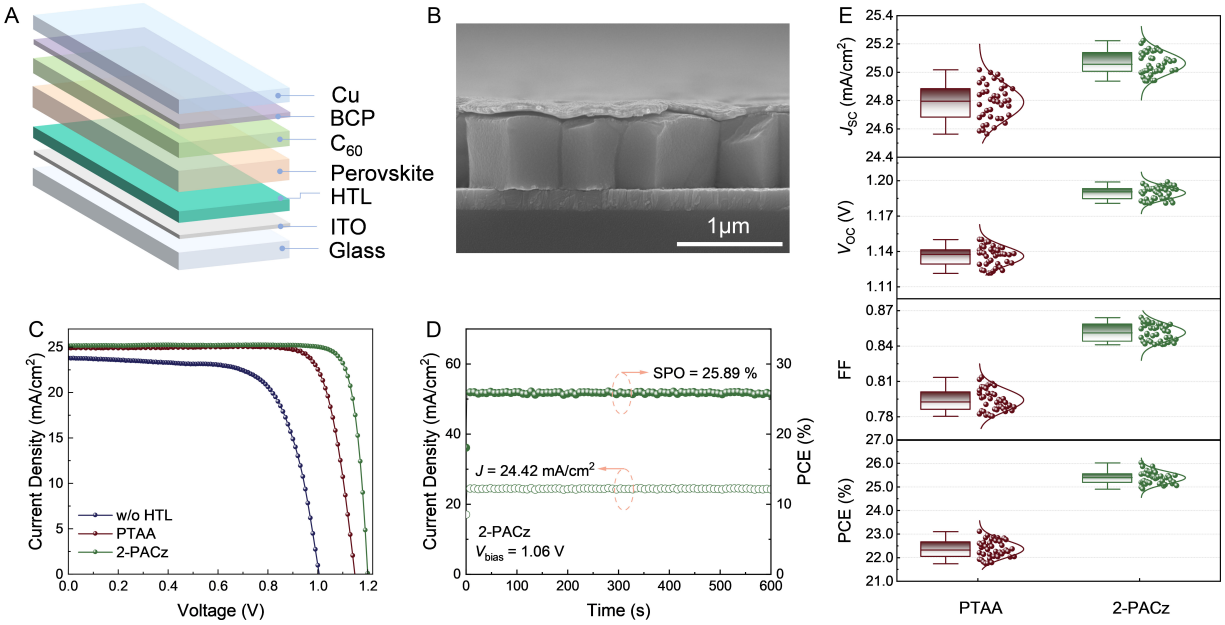

Figure 4. Device configuration and performance. (A) the device architecture of the p-i-n perovskite solar cells; (B) Cross-sectional SEM micrograph of the p-i-n PSCs. The scale bar is 1 μm; (C) *J-V* curves of devices without HTL, PVK/PTAA, and PVK/2-PACz; (D) The stabilized output of the champion device measured at the maximum power point (MPP) for 600 s. The applied bias voltage is 1.06 V, and the stabilized current density is 24.42 mA/cm², resulting in a stabilized PCE of 25.89%. A stabilized PCE of 25.89% was recorded for the 2-PACz-based device by tracking its output at the MPP under sustained one-sun illumination; (E) Statistics of the photovoltaic performance parameters (PCE, J_{SC}, V_{OC}, and *FF*) for PSCs based on 2-PACz versus PTAA HTLs. BCP: 2,9-Dimethyl-4,7-diphenyl-1,10-phenanthroline; HTL: hole transport layer; ITO: indium tin oxide; PTAA: poly[bis(4-phenyl)(2,4,6-triMethylphenyl)aMine]; 2-PACz: [2-(9H-carbazol-9-yl)ethyl]phosphonic acid; SPO: steady-state power output efficiency; PCE: power conversion efficiency; FF: fill factor; V_{OC}: open-circuit voltage; J_{SC}: short-circuit current; *J-V*: current density-voltage; SEM: scanning electron microscopy; PSC: perovskite solar cell.

Table 1. Photovoltaic parameters of PSCs with different HTLs

HTL	J_{SC} (mA/cm²)	V_{OC} (V)	FF (%)	PCE (%)
w/o HTL	24.81	1.01	69.1	17.32
PTAA	24.91	1.15	80.7	23.12
2-PACz	25.16	1.20	86.2	26.03

HTL: Hole transport layer; J_{SC}: short-circuit current; V_{OC}: open-circuit voltage; FF: fill factor; PCE: power conversion efficiency; PTAA: poly[bis(4-phenyl)(2,4,6-triMethylphenyl)aMine]; 2-PACz: [2-(9H-carbazol-9-yl)ethyl]phosphonic acid.

good reproducibility, with an average PCE of 25.39% and V_{OC} of 1.190 V, whereas PTAA-based PSCs showed an average PCE of 22.37% and V_{OC} of 1.136V. These results clearly demonstrate the superior performance of 2-PACz as an HTL. The performance enhancement arises mainly from reduced non-radiative recombination losses in the PVK/2-PACz system. Compared to traditional PTAA, 2-PACz improves film uniformity and interfacial quality. As shown in Figure 1A, the PVK/2-PACz interface exhibits enhanced PL intensity due to effective defect passivation. This leads to higher fill factor (FF) and V_{OC}, boosting the overall device efficiency. The nearly unchanged J_{SC} values, together with the substantial increases in V_{OC} and FF, indicate that suppression of interfacial non-radiative recombination is the primary contributor to the improved device performance. TAS measurements further suggest that more efficient interfacial carrier transfer in PVK/2-PACz helps reduce charge accumulation and supports efficient device operation[48].

To further evaluate the device performance of solar cells with different HTLs under high carrier densities, we tested concentrator solar cells using lenses to focus light from a solar simulator. Performance metrics for PTAA-based and 2-PACz-based devices under 1 sun and 5 sun illumination are summarized in Table 2. The

Table 2. Photovoltaic parameters of PSCs with different HTL under different solar intensity

Solar intensity	HTL	J_{sc} (mA/cm²)	V_{oc} (V)	FF (%)	PCE (%)
1 sun	PTAA	24.91	1.15	80.7	23.12
	2-PACz	25.16	1.20	86.2	26.03
5 sun	PTAA	124.7	1.23	80.6	24.73
	2-PACz	125.6	1.27	85.4	27.24

HTL: Hole transport layer; J_{SC}: short-circuit current; V_{OC}: open-circuit voltage; FF: fill factor; PCE: power conversion efficiency; PTAA: poly[bis(4-phenyl)(2,4,6-triMethylphenyl)aMine]; 2-PACz: [2-(9H-carbazol-9-yl)ethyl]phosphonic acid.

2-PACz-based device exhibits a V_{OC} of 1.27 V under 5 suns, with a corresponding PCE of 27.24%, significantly higher than the 26.03% PCE observed under 1 sun. In contrast, the PTAA-based solar cell shows an increase in PCE from 23.12% under 1 sun to 24.73% under 5 suns. However, the performance of the PTAA-based device remains slightly inferior to that of the 2-PACz-based device. As the intensity of the sun increases, the radiant temperature rises [Supplementary Figure 8]. To reduce the temperature effect on the device and further verify the influence of light irradiation, we tested the photocurrent of perovskite solar cells with varying light intensities of a 660nm laser [Supplementary Figure 9]. We found that compared to devices without HTL and those with PTAA, the device with a 2-PACz hole transport layer exhibited the highest current and the steepest slope with changing light intensity, indicating better photoresponse and fewer non-radiative recombination losses.

Although the present study focuses on ultrafast spectroscopic investigations of HTL-dependent carrier dynamics, complementary electrical transient measurements, including transient photovoltage, transient photocurrent, and space-charge-limited current analysis, could provide further insight into carrier transport and recombination under device operating conditions and will be the subject of future work.

CONCLUSIONS

In conclusion, we show that HTLs simultaneously influence interfacial passivation, carrier transfer, and polaronic relaxation in metal halide perovskites. PTAA is associated with increased interfacial non-radiative recombination, whereas 2-PACz effectively passivates interfacial defects and promotes carrier transfer across the PVK/HTL interface. Under high excitation densities, a second bleach feature emerges that is consistent with HTL-facilitated polaron formation, leading to modified carrier relaxation dynamics through enhanced screening of electron-hole interactions. These interfacial effects correlate with improved photovoltaic performance, enabling 2-PACz-based devices to achieve PCEs of 26.03% (stabilized 25.89%) under one-sun illumination and 27.24% under 5-sun concentration. Our results highlight interfacial control of carrier and polaron dynamics as an effective strategy for advancing high-performance perovskite photovoltaics.

DECLARATIONS

Authors' contributions

Validation: Niu, X.; Zhu, P.
Conceptualization: Zhang, Y.; He, F.
Methodology: He, F.
Visualization: Zeng, J.
Software: Zeng, J.
Data Curation: Pang, R.
Formal analysis: Wang, S.
Investigation: Wang, S.
Supervision: Xu, B.
Writing - original draft: Niu, X.; Zhu, P.
Writing - review & editing: Pang, R.; Zhang, Y.; He, F.

Funding acquisition: Zhu, P.; Zhang, Y.; He, F.

Availability of data and materials

The original contributions presented in this study are included in the article/Supplementary Materials. Further inquiries can be directed to the corresponding authors.

AI and AI-assisted tools statement

Not applicable.

Financial support and sponsorship

He, F. acknowledges funding support from the Shenzhen Science and Technology Program (Grant No. JCYJ20240813104828038). Zhang, Y. acknowledges the Youth S&T Talent Support Programme of Guangdong Provincial Association for Science and Technology (GDSTA) (No. SKXRC2025469). Zhu, P. acknowledges funding support from the National Natural Science Foundation of China (Grant No. 224B2904).

Conflicts of interest

All authors declared that there are no conflicts of interest.

Ethical approval and consent to participate

Not applicable.

Consent for publication

Not applicable.

Copyright

© The Author(s) 2026.

Supplementary Materials

Supplementary Materials

REFERENCES

1. Yang, Y.; Ostrowski, D. P.; France, R. M.; et al. Observation of a hot-phonon bottleneck in lead-iodide perovskites. *Nat. Photonics.* **2016**, *10*, 53-9. DOI
2. Price, M. B.; Butkus, J.; Jellicoe, T. C.; et al. Hot-carrier cooling and photoinduced refractive index changes in organic-inorganic lead halide perovskites. *Nat. Commun.* **2015**, *6*, 8420. DOI PubMed PMC
3. Bretschneider, S. A.; Ivanov, I.; Wang, H. I.; Miyata, K.; Zhu, X.; Bonn, M. Quantifying polaron formation and charge carrier cooling in lead-iodide perovskites. *Adv. Mater.* **2018**, , e1707312. DOI PubMed
4. Joshi, P. P.; Maehrlein, S. F.; Zhu, X. Dynamic screening and slow cooling of hot carriers in lead halide perovskites. *Adv. Mater.* **2019**, *31*, e1803054. DOI PubMed
5. Mosquera-Lois, I.; Huang, Y. T.; Lohan, H.; Ye, J.; Walsh, A.; Hoye, R. L. Z. Multifaceted nature of defect tolerance in halide perovskites and emerging semiconductors. *Nat. Rev. Chem.* **2025**, *9*, 287-304. DOI PubMed
6. Xu, N.; Qi, X.; Shen, Z.; et al. Point defects in metal halide perovskites. *Nat. Rev. Phys.* **2025**, *7*, 554-64. DOI
7. Zhu, P.; Wang, D.; Zhang, Y.; et al. Aqueous synthesis of perovskite precursors for highly efficient perovskite solar cells. *Science* **2024**, *383*, 524-31. DOI
8. Zhang, X.; Wu, S.; Zhang, H.; Jen, A. K. Y.; Zhan, Y.; Chu, J. Advances in inverted perovskite solar cells. *Nat. Photonics.* **2024**, *18*, 1243-53. DOI
9. Cao, Y. B.; Zhang, D.; Zhang, Q.; et al. High-efficiency, flexible and large-area red/green/blue all-inorganic metal halide perovskite quantum wires-based light-emitting diodes. *Nat. Commun.* **2023**, *14*, 4611. DOI PubMed PMC
10. Dong, H.; Ran, C.; Gao, W.; Li, M.; Xia, Y.; Huang, W. Metal halide perovskite for next-generation optoelectronics: progresses and prospects. *eLight* **2023**, *3*, 33. DOI
11. Haque, M. A.; Beard, M. C. Spin effects in metal halide perovskite semiconductors. *Nanoscale* **2025**, *17*, 9895-906. DOI PubMed
12. Liu, S.; Li, J.; Xiao, W.; et al. Buried interface molecular hybrid for inverted perovskite solar cells. *Nature* **2024**, *632*, 536-42. DOI

13. Zhang, S.; Ye, F.; Wang, X.; et al. Minimizing buried interfacial defects for efficient inverted perovskite solar cells. *Science* **2023**, *380*, 404-9. DOI
14. Li, Z.; Sun, X.; Zheng, X.; et al. Stabilized hole-selective layer for high-performance inverted p-i-n perovskite solar cells. *Science* **2023**, *382*, 284-9. DOI
15. Dursun, I.; Maity, P.; Yin, J.; et al. why are hot holes easier to extract than hot electrons from methylammonium lead iodide perovskite? *Adv. Energy. Mater.* **2019**, *9*, 1900084. DOI
16. Khan, J. I.; Isikgor, F. H.; Ugur, E.; et al. Charge carrier recombination at perovskite/hole transport layer interfaces monitored by time-resolved spectroscopy. *ACS. Energy. Lett.* **2021**, *6*, 4155-64. DOI
17. Yu, S.; Xiong, Z.; Zhou, H.; et al. Homogenized NiO_x nanoparticles for improved hole transport in inverted perovskite solar cells. *Science* **2023**, *382*, 1399-404. DOI
18. Kirchartz, T.; Márquez, J. A.; Stolterfoht, M.; Unold, T. Photoluminescence-based characterization of halide perovskites for photovoltaics. *Adv. Energy. Mater.* **2020**, *10*, 1904134. DOI
19. Xu, W.; Hart, L. J. F.; Moss, B.; et al. Impact of interface energetic alignment and mobile ions on charge carrier accumulation and extraction in p-i-n perovskite solar cells. *Adv. Energy. Mater.* **2023**, *13*, 2301102. DOI
20. Li, Y.; Wang, B.; Liu, T.; et al. Interfacial engineering of PTAA/perovskites for improved crystallinity and hole extraction in inverted perovskite solar cells. *ACS. Appl. Mater. Interfaces.* **2022**, *14*, 3284-92. DOI
21. Park, S. M.; Wei, M.; Lempesis, N.; et al. Low-loss contacts on textured substrates for inverted perovskite solar cells. *Nature* **2023**, *624*, 289-94. DOI
22. Mariotti, S.; Rabehi, I. N.; Zhang, C.; et al. Unraveling the morphological and energetic properties of 2PACz self-assembled monolayers fabricated with upscaling deposition methods. *Energy. Environ. Mater.* **2025**, *8*, e12825. DOI
23. Knowles, K. E.; Koch, M. D.; Shelton, J. L. Three applications of ultrafast transient absorption spectroscopy of semiconductor thin films: spectroelectrochemistry, microscopy, and identification of thermal contributions. *J. Mater. Chem. C.* **2018**, *6*, 11853-67. DOI
24. Liu, X.; Zeng, P.; Chen, S.; Smith, T. A.; Liu, M. Charge Transfer dynamics at the interface of $CsPbX_3$ perovskite nanocrystal-acceptor complexes: a femtosecond transient absorption spectroscopy study. *Laser. Photonics. Rev.* **2022**, *16*, 2200280. DOI
25. Niedzwiedzki, D. M.; Kouhnavard, M.; Diao, Y.; D'Arcy, J. M.; Biswas, P. Spectroscopic investigations of electron and hole dynamics in $MAPbBr_3$ perovskite film and carrier extraction to PEDOT hole transport layer. *Phys. Chem. Chem. Phys.* **2021**, *23*, 13011-22. DOI PubMed
26. Zheng, K.; Žídek, K.; Abdellah, M.; et al. High excitation intensity opens a new trapping channel in organic-inorganic hybrid perovskite nanoparticles. *ACS. Energy. Lett.* **2016**, *1*, 1154-61. DOI
27. Cappel, U. B.; Feldt, S. M.; Schöneboom, J.; Hagfeldt, A.; Boschloo, G. The influence of local electric fields on photoinduced absorption in dye-sensitized solar cells. *J. Am. Chem. Soc.* **2010**, *132*, 9096-101. DOI
28. Trinh, M. T.; Wu, X.; Niesner, D.; Zhu, X. Many-body interactions in photo-excited lead iodide perovskite. *J. Mater. Chem. A.* **2015**, *3*, 9285-90. DOI
29. Pydzińska, K.; Karolczak, J.; Kosta, I.; et al. Determination of interfacial charge-transfer rate constants in perovskite solar cells. *ChemSusChem* **2016**, *9*, 1647-59. DOI
30. Mondal, N.; De, A.; Das, S.; Paul, S.; Samanta, A. Ultrafast carrier dynamics of metal halide perovskite nanocrystals and perovskite-composites. *Nanoscale* **2019**, *11*, 9796-818. DOI PubMed
31. Ahmed, I.; Shi, L.; Pasanen, H.; et al. There is plenty of room at the top: generation of hot charge carriers and their applications in perovskite and other semiconductor-based optoelectronic devices. *Light. Sci. Appl.* **2021**, *10*, 174. DOI PubMed PMC
32. Chen, X.; Kamat, P. V.; Janáky, C.; Samu, G. F. Charge transfer kinetics in halide perovskites: on the constraints of time-resolved spectroscopy measurements. *ACS. Energy. Lett.* **2024**, *9*, 3187-203. DOI PubMed PMC
33. Shi, J.; Li, Y.; Li, Y.; et al. From ultrafast to ultraslow: charge-carrier dynamics of perovskite solar cells. *Joule* **2018**, *2*, 879-901. DOI
34. Musiienko, A.; Ceratti, D. R.; Pipek, J.; et al. Defects in hybrid perovskites: the secret of efficient charge transport. *Adv. Funct. Mater.* **2021**, *31*, 2104467. DOI
35. Butler-Caddle, E.; Jayawardena, K. I.; Wijesekara, A.; Milot, R. L.; Lloyd-Hughes, J. Distinguishing carrier transport and interfacial recombination at perovskite/transport-layer interfaces using ultrafast spectroscopy and numerical simulation. *Phys. Rev. Appl.* **2024**, *22*, 024013. DOI
36. Ugur, E.; Khan, J. I.; Aydin, E.; et al. Carrier extraction from perovskite to polymeric charge transport layers probed by ultrafast transient absorption spectroscopy. *J. Phys. Chem. Lett.* **2019**, *10*, 6921-8. DOI
37. Xing, G.; Wu, B.; Chen, S.; et al. Interfacial electron transfer barrier at compact TiO_2/$CH_3NH_3PbI_3$ heterojunction. *Small* **2015**, *11*, 3606-13. DOI
38. Manser, J. S.; Kamat, P. V. Band filling with free charge carriers in organometal halide perovskites. *Nat. Photon.* **2014**, *8*, 737-43. DOI

39. Franchini, C.; Reticcioli, M.; Setvin, M.; Diebold, U. Polarons in materials. *Nat. Rev. Mater.* **2021**, *6*, 560-86. DOI
40. Miyata, K.; Meggiolaro, D.; Trinh, M. T.; et al. Large polarons in lead halide perovskites. *Sci. Adv.* **2017**, *3*, e1701217. DOI PubMed PMC
41. Even, J.; Pedesseau, L.; Jancu, J.; Katan, C. Importance of spin-orbit coupling in hybrid organic/inorganic perovskites for photovoltaic applications. *J. Phys. Chem. Lett.* **2013**, *4*, 2999-3005. DOI
42. Yu, Z. G. Rashba effect and carrier mobility in hybrid organic-inorganic perovskites. *J. Phys. Chem. Lett.* **2016**, *7*, 3078-83. DOI PubMed
43. Kepenekian, M.; Robles, R.; Katan, C.; Sapori, D.; Pedesseau, L.; Even, J. Rashba and Dresselhaus effects in hybrid organic-inorganic perovskites: from basics to devices. *ACS. Nano.* **2015**, *9*, 11557-67. DOI PubMed
44. Zhang, H.; Park, N. Polarons in perovskite solar cells: effects on photovoltaic performance and stability. *J. Phys. Energy.* **2023**, *5*, 024002. DOI
45. Li, M.; Fu, J.; Xu, Q.; Sum, T. C. Slow hot-carrier cooling in halide perovskites: prospects for hot-carrier solar cells. *Adv. Mater.* **2019**, *31*, e1802486. DOI
46. Jin, Z.; Peng, Y.; Fang, Y.; et al. Photoinduced large polaron transport and dynamics in organic-inorganic hybrid lead halide perovskite with terahertz probes. *Light. Sci. Appl.* **2022**, *11*, 209. DOI PubMed PMC
47. Wilcken, R.; Esses, B. L.; Nithyananda, Kumar. R. S.; Hurley, L. A.; Shaheen, S. E.; Raschke, M. B. Correlated nanoimaging of structure and dynamics of cation-polaron coupling in hybrid perovskites. *Sci. Adv.* **2025**, *11*, eads3706. DOI PubMed PMC
48. Stolterfoht, M.; Wolff, C. M.; Amir, Y.; et al. Approaching the fill factor Shockley-Queisser limit in stable, dopant-free triple cation perovskite solar cells. *Energy. Environ. Sci.* **2017**, *10*, 1530-9. DOI

Disclaimer/Publisher's Note: All statements, opinions, and data contained in this publication are solely those of the individual author(s) and contributor(s) and do not necessarily reflect those of OAE and/or the editor(s). OAE and/or the editor(s) disclaim any responsibility for harm to persons or property resulting from the use of any ideas, methods, instructions, or products mentioned in the content.

© The Author(s) 2026. Open Access This article is licensed under a Creative Commons Attribution 4.0 International License (https://creativecommons.org/licenses/by/4.0/), which permits unrestricted use, sharing, adaptation, distribution and reproduction in any medium or format, for any purpose, even commercially, as long as you give appropriate credit to the original author(s) and the source, provide a link to the Creative Commons license, and indicate if changes were made.